Oxidation Behavior and Creep Resistance of Cast MC-Strengthened CoNiFeMnCr HEAs at 1100 °C

Patrice Berthod, Lionel Aranda

micro

MDPI

Article

Oxidation Behavior and Creep Resistance of Cast MC-Strengthened CoNiFeMnCr HEAs at 1100 °C

Patrice Berthod [1,2,*] and Lionel Aranda [1]

[1] Institut Jean Lamour, CNRS, 2 Allée André Guinier, Campus Artem, 54000 Nancy, France; lionel.aranda@univ-lorraine.fr
[2] Faculté des Sciences et Technologies, Université de Lorraine, Campus Victor Grignard, 54500 Vandoeuvre-lès-Nancy, France
* Correspondence: patrice.berthod@univ-lorraine.fr; Tel.: +33-3-72-74-27-29

Abstract: The reinforcement of cast Cantor's-type high-entropy alloys by MC carbides and their effect on the hot oxidation behavior were investigated. Three equimolar CoNiFeMnCr alloys without or with carbon and with either hafnium or tantalum were elaborated. Their as-cast microstructures were specified. Oxidation tests were carried out in air at 1100 °C. Flexural creep tests were performed at 1100 °C at 10 MPa. The carbide-free CoNiFeMnCr alloy was single-phased. The version with Hf and C added and the one with Ta and C added contained interdendritic eutectic script HfC and TaC carbides, respectively. After oxidation for 50 h at 1100 °C, all alloys were covered by a $(Cr,Mn)_2O_3$ scale with various proportions of Cr and Mn. HfO_2 or $CrTaO_4$ also formed. Oxidation resulted in a deep depletion in Cr and in Mn in the subsurface. Oxidation is much faster for the three alloys by comparison with chromia-forming alloys. Their bad oxidation behavior is obviously due to Mn and protection by coating is to be considered. The creep deformation of the carbide-free CoNiFeMnCr alloy was very fast. The creep resistance of the two versions reinforced by either HfC or TaC deformed much slower. The addition of these MC carbides led to a deformation rate divided by five to ten times. Now, creep behavior comparisons with commercial alloys are to be conducted. They will be performed soon.

Keywords: HEA alloys; equimolar CoNiFeMnCr; HfC; TaC; high temperature; oxidation; creep

Citation: Berthod, P.; Aranda, L. Oxidation Behavior and Creep Resistance of Cast MC-Strengthened CoNiFeMnCr HEAs at 1100 °C. *Micro* **2024**, *4*, 751–764. https://doi.org/10.3390/micro4040046

Academic Editor: Kiryl Yasakau

Received: 26 September 2024
Revised: 12 November 2024
Accepted: 20 November 2024
Published: 3 December 2024

1. Introduction

During the last 20 years, special attention has been given to a new metallurgical principle: high-entropy alloys (HEAs) or multi-principal element alloys (MEAs) [1]. Among the alloys that are close to high-temperature alloys, there are the alloys which combine the classical base elements of superalloys—namely nickel, iron and cobalt—and the elements bringing oxidation and corrosion resistance: aluminum and chromium [2]. One type with specially designed chemical compositions is eutectic high-entropy alloys [3]. Other elements, such as Ti [4,5] or Cu and even Ag and B [6], can also be involved in HEA compositions. One of the most common element associations met for HEAs is the Co–Ni–Fe–Mn–Cr combination [7–9]. This association of five elements has also been found in combination with oxygen to obtain high-entropy oxides [10]. Many of the HEAs involving Co, Ni, Fe, Mn and Cr are designed to respect a molar equivalence for the five elements [11–13]. These equimolar CoNiFeMnCr HEAs can be produced using various elaboration techniques. One can cite advanced or recent technologies such as single-crystalline structure generation [14] and additive manufacturing [15] for bulk materials. Coatings may also be realized with these particular HEAs [16]. Much attention has been paid to these equimolar CoNiFeMnCr alloys. Notably, their thermodynamic properties [17], their mechanical strength and strengthening possibilities [18,19] and the diffusion phenomena in this system [20,21] have been studied. CoNiFeMnCr alloys in general, and equimolar alloys in particular, are also easily castable. Conventional melting may lead to polycrystalline equiaxed alloys

demonstrating interesting oxidation and mechanical behaviors at moderate temperatures. Furthermore, due to their high melting start temperatures, they can be considered for uses in hot working conditions. However, one may worry about their properties. Notably, low mechanical resistance can be feared because of the absence of phases able to strengthen intergrain and interdendrite spaces. For such purposes, primary carbides—and notably MC carbides—have previously demonstrated favorable influence on high-temperature mechanical properties in the case of chromium-rich nickel-based and cobalt-based model alloys [22] or superalloys [23]. To achieve such reinforcement, carbon and carbide former elements must be present in significant quantities in the concerned alloys.

Concerning specifically high-entropy alloys, the presence of carbon in their chemical composition is exceptional (an example of such an exception: [24]). Until today, to our knowledge, C had never been introduced in HEAs in association with Ta or Hf, elements which lead to particularly efficient carbides for strengthening alloys at high temperatures. Very recently, the microstructural consequences of the (0.25–0.50 C, 3.7–7.4 Ta or Hf, in wt.%) addition to a conventionally cast CoNiFeMnCr equimolar alloy have been investigated (e.g., [25]); this promoted the formation, in the interdendritic spaces, of script-like eutectic TaC or HfC carbides.

The purpose of the present work is to explore the behavior of these new MC-containing CoNiFeMnCr-based alloy properties considering high-temperature, mechanical (strength) and chemical (oxidation) factors. Special attention will be paid to the strengthening potential of the interdendritic TaC and HfC carbides in situations of creep at temperatures as high as 1100 °C and to the consequences of their presence on the resistance of the alloy against hot oxidation.

2. Materials and Methods

A CoNiFeMnCr equimolar alloy and two of the MC-containing HEAs recently obtained for as-cast microstructure examinations (e.g., [25]) were produced. One targeted the same chemical compositions and one followed the same synthesis procedure. This procedure is described in the following sentences. Initially, the adequate quantities of pure elements (>99.5 wt.%) were accurately weighed, using a precision balance. The elements were placed in the copper crucible of a furnace. This one was thereafter isolated from ambient air by a silica tube closing the fusion chamber. Pumping was performed to decrease the internal pressure down to about 4×10^{-2} mbars. Pure argon was then introduced into the chamber until 300 mbars of argon was reached. This pumping, Ar introduction sequence was repeated three times. Heating and melting were achieved by applying a 100 kHz alternative current in the external coil surrounding the silica tube and the crucible. The metallic parts were heated due to the induced Foucault's currents and the resulting Joule effect. At the same time, the copper crucible and coil were continuously cooled by internal water circulation. After complete melting, the temperature of the liquid alloy was maintained for 10 min at about 1600 °C for its chemical homogenization. Liquid-state cooling, solidification and solid-state cooling were realized by decreasing the input power. About 30 minutes later, the fusion chamber was opened and the obtained ingot was extracted from the crucible. After classical metallographic preparation, the chemical composition and the as-cast microstructure were controlled using a scanning electron microscope JSM6010-LA (SEM) and an energy-dispersive spectrometer (EDS), both from JEOL (Tokyo, Japan).

Per alloy, a sample was prepared with the following approximative dimensions: thickness = 3 mm; widths or lengths = 10 mm. The surface state was obtained by grinding using #1200 SiC papers (edges and corners smoothed with the same papers). Each sample was tested in oxidation in a muffle-resistive furnace (conditions: 50 h at 1100 °C; laboratory air). Tests were followed by classical postmortem characterization: (1) X-ray diffraction (XRD) on the oxidized surfaces (D8 Advance diffractometer, from Bruker, Billerica, MA, USA) using the Cu Kα radiation (wavelength = 0.15406 nm) and analysis of the results using the Diffrac.Eva 5.0 software, (2) embedding in a cold resin system, (3) precision cutting of the embedded oxidized sample in two halves, (4) grinding and polishing to

obtain a mirror-like state, (5) SEM observation of the oxides in the back-scattered electrons mode (BSE) at various magnifications, (6) SEM observation in BSE mode of the subsurfaces affected by oxidation and of the bulks affected by the high-temperature exposure, (7) EDS spot analysis and concentration profiles, and (8) EDS elemental mapping.

Per alloy again, another sample was cut to obtain a parallelepiped shape (approximative dimensions: thickness = 1.5 mm; width or length = 2 and 15 mm). Its surface state was especially prepared by grinding using #1200 SiC papers. This sample was subjected to a centered three-point bending under a load, leading to a maximal 10 MPa local tensile stress, calculated according to the equation of the elasticity theory. The progress of the displacement at 1100 °C under this constant load of the central point was monitored using a precision sensor.

3. Results and Discussion

3.1. Chemical Compositions

Preliminarily, the chemical compositions of the three alloys were measured (Table 1). According to the chosen atomic contents in Co, Ni, Fe, Mn and Cr (intended to all be equal to one another), the weight contents of these five elements (the molar weights of which are close to one another) are logically very similar. This is true for the quinary CoNiFeMnCr alloy (named "HEAbase") as well as for the two alloys containing either Hf or Ta (named "HEAhfc" and "HEAtac", respectively). In the latter alloys, the Hf and Ta weight contents are a little higher than targeted contents. Such small overestimation is usual when coarse HfC or TaC is present.

Table 1. Designation and controlled chemical compositions of the three alloys (from five ×250 full frame EDS analyses per alloy); weight and atomic contents in all elements except carbon (for C: 0.25 wt.% and 1.2 at.% for both the HEAhfc and HEAtac alloys).

Weight and Atomic Contents		Cr	Mn	Fe	Co	Ni	Hf or Ta
HEAbase	wt.%	19.8	19.5	19.5	19.8	21.4	/
	at.%	20.1	20.2	19.9	19.1	20.7	/
HEAhfc	wt.%	19.3	18.2	18.4	19.9	20.2	4.0
	at.%	19.9	19.1	19.0	19.5	19.9	1.3
HEAtac	wt.%	19.2	18.3	18.6	19.3	20.1	4.5
	at.%	19.9	19.3	19.3	19.0	19.9	1.4

3.2. As-Cast Microstructures

The as-cast "HEAbase" alloy (Figure 1), prepared to serve as reference for identifying the effects of the presence of either HfC or TaC in the behaviors of the other alloys, is obviously single-phased and rather homogeneous chemically. Concerning the second observation, one must mention that Mn segregation seems to have occurred during solidification. Such a phenomenon was already noticed and studied in CoNiFeMnCr alloys [26]. The Mn-enriched zones allow the dendritic structure of this alloy to be distinguished.

The as-cast "HEAhfc" and "HEAtac" alloys (Figure 2 and Figure 3, respectively) are obviously double-phased. Their microstructures are composed of a dendritic matrix and of an interdendritic carbide network made of HfC carbides or TaC carbides, respectively. The identification of these carbides was conducted by carrying out EDS spot analysis on the coarsest carbides found in the metallographic samples. In addition to these script-like eutectic carbides, both alloys also contain some coarse carbides. Obviously, these ones precipitated prior to the eutectic solidification and to the pre-eutectic development of the dendritic matrix. One can remark that manganese segregation during solidification took place also for these two alloys.

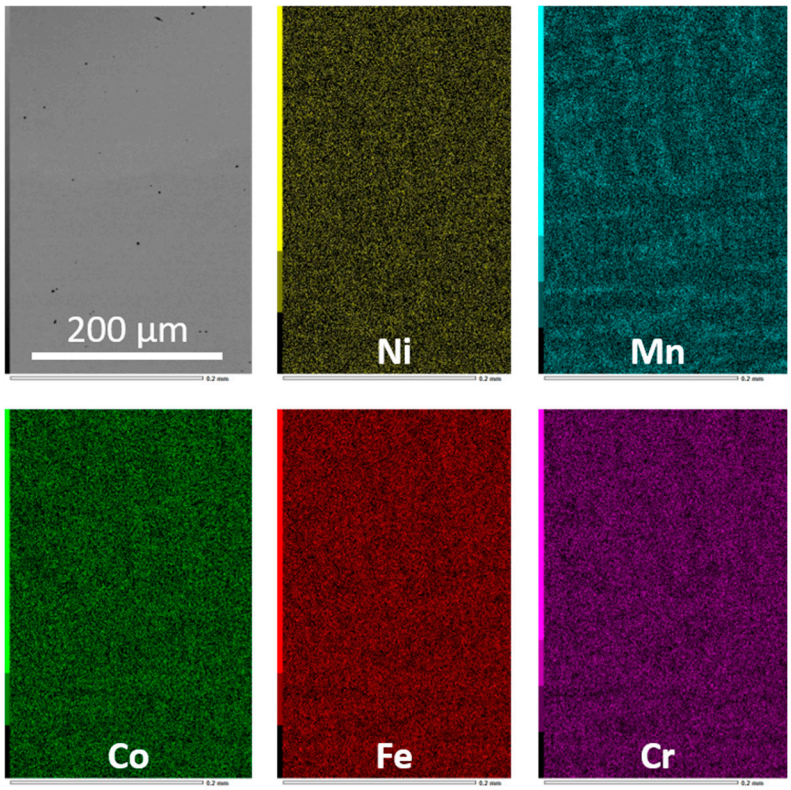

Figure 1. As-cast microstructure of the HEAbase alloy (SEM/BSE image and elemental mapping).

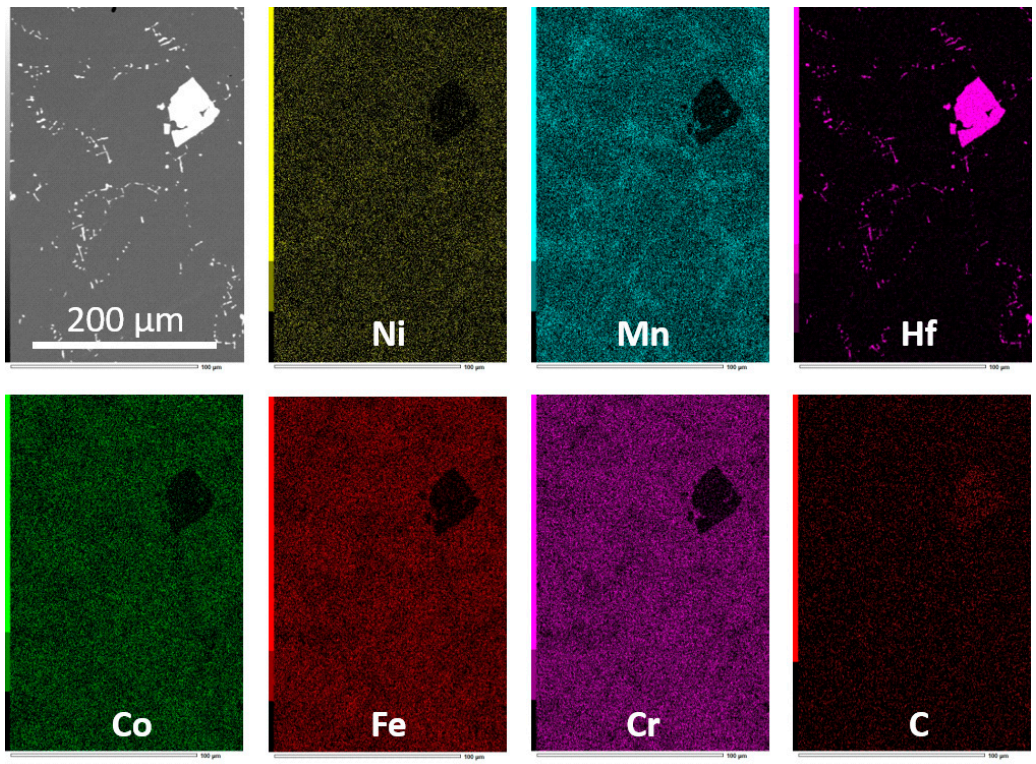

Figure 2. As-cast microstructure of the HEAhfc alloy (SEM/BSE image and elemental mapping).

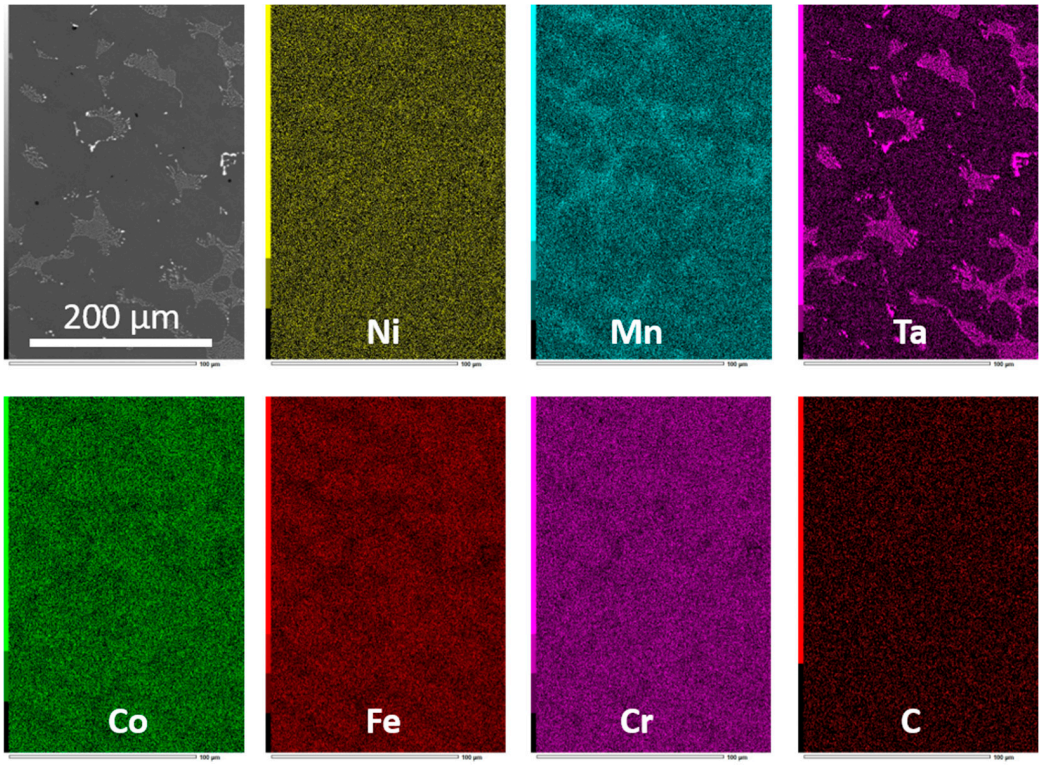

Figure 3. As-cast microstructure of the HEAtac alloy (SEM/BSE image and elemental mapping).

3.3. Postmortem Characterization of the Oxidized Samples

Prior to embedding and cross-section preparations, X-ray diffraction was performed on the surfaces of the oxidized samples. The obtained diffractograms were not easy to exploit since several obtained peaks were difficult to identify. Nevertheless one can estimate that chromia, (Mn,Cr)-rich oxides and (Co,Ni)Cr_2O_4 spinel oxides formed on the surfaces of the three alloys during the 50 h spent at 1100 °C (Figure 4 for HEAbase, Figure 5 for HEAhfc and Figure 6 for HEAtac). The additional presence of discrete HfO_2 was detected in the case of the HEAhfc alloy. $CrTaO_4$ mixed oxide was evidenced in the case of the HEAtac alloy.

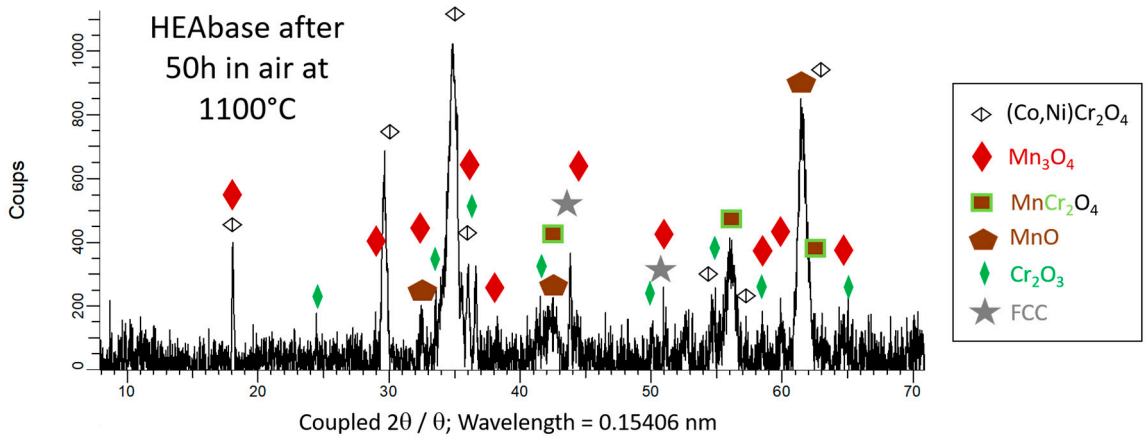

Figure 4. Diffractogram acquired of one of the oxidized surfaces of the HEAbase alloy.

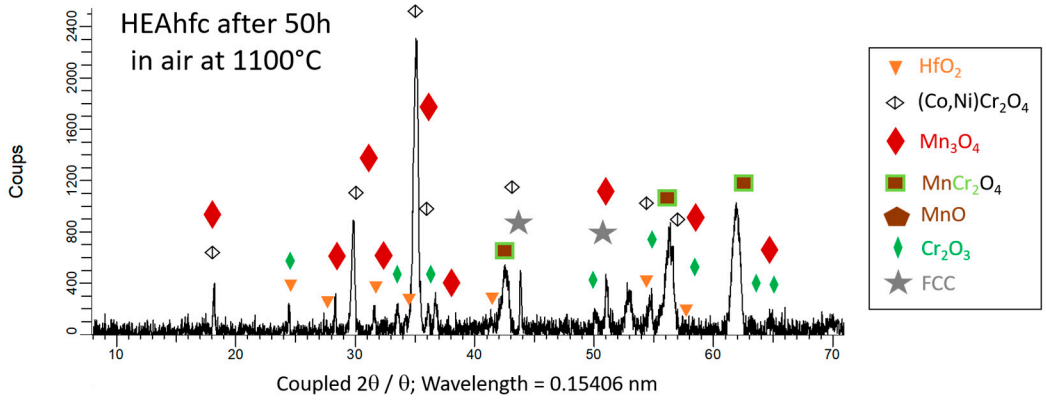

Figure 5. Diffractogram acquired of one of the oxidized surfaces of the HEAhfc alloy.

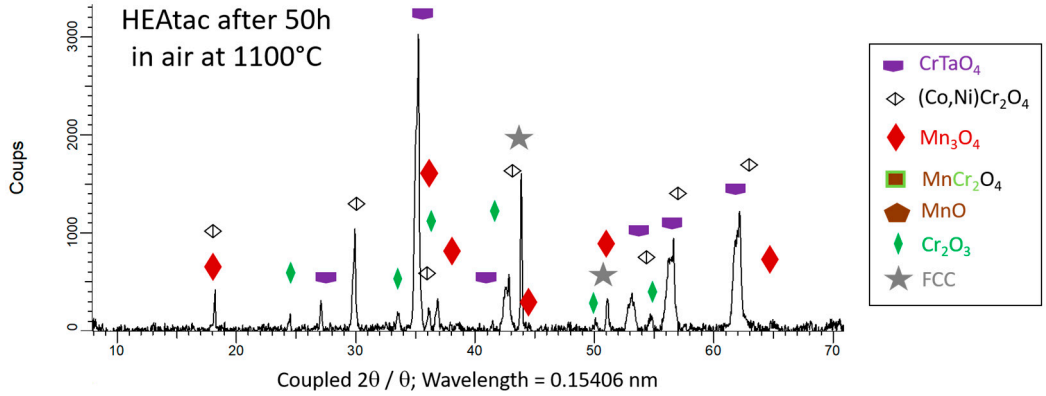

Figure 6. Diffractogram acquired of one of the oxidized surfaces of the HEAtac alloy.

The investigations about the natures of the oxides present were carried out further with the observation of the oxidized states of the surfaces and subsurfaces in the cross-sectional samples. On low magnification SEM/BSE micrographs (Figure 7), one can see that parts of the external oxide scales were preserved and are available for observation and characterization. The average thickness of the continuous oxide scale covering the alloys is about 20–25 µm, measured where the whole scale—or at least the main part of the initial scale—is still present (no loss by local spallation at cooling). This is twice (or more) the one generally observed for chromia-forming alloy in the same test conditions (i.e., oxidizing atmosphere, temperature and duration).

These micrographs also allow the examination of the subsurfaces affected by oxidation; inward progression of oxidation took place for the three alloys, especially for the HEAbase alloy for which local very deep progression of oxidation may be noticed here and there. Other phenomena also occurred as the inward development of a carbide-free zone from the oxidation front. This is a classical phenomenon for many carbide-containing polycrystalline cast alloys and superalloys (e.g., [27]). One can also note the appearance of porosities in the same area, especially for the HEAbase alloy. This probably results from the Kirdendall effect. This effect was already observed for CoNiFeMnCr alloys during oxidation at temperatures of the 1000 °C level [28].

At higher magnification (Figure 8), one can distinguish gray gradation among the (Mn,Cr) oxides. According to a series of EDS spot analyses, these ones appear to be of the M_2O_3 stoichiometry, M representing Mn and Cr essentially. The darkest parts of these oxides are richer in chromium than in manganese (about twice more Cr than Mn). Furthermore, one can say that the chromia stoichiometry is almost obtained for the darkest oxides located very close to the alloy. The pale parts are richer in Mn than in Cr (about twice more Mn than Cr). The formations of $Mn(Cr)_2O_3$ and Cr_2O_3 were previously reported in the case of the CoNiFeMnCr alloy but after oxidation at 900 °C [28]. In the same work,

in which the oxidation of this alloy was also studied at 1000 and 1100 °C, it appeared that there were more mixed oxides of Mn and Cr with the $(Mn,Cr)_3O_4$ stoichiometry that were seen. Nevertheless, one may insist on the good agreement concerning the simultaneous and important participation of both Cr and Mn in the external oxidation phenomenon.

General chemical information about the results of oxidation on the surface and in the subsurface is provided by EDS elemental cartography. Some X-maps are available in Figures 9–11 for the HEAbase alloy, the HEAhfc alloy and the HEAtac alloy, respectively. They efficiently illustrate the variations in Cr and Mn contents in the external oxide scales, as described above in the text (all alloys, particularly in Figures 10 and 11) and in the deep oxidation penetration affecting the HEAbase here and there (Figure 9). One can also see the progressive oxidation of the HfC carbides (Figure 10) and of the TaC carbides (Figure 11) in the subsurface (the carbide core is still unaffected, while its periphery is oxidized). In addition, the X-maps also allow visualization of the subsurface zone depleted in chromium and in hafnium. This is more visible in Figure 9 than in Figures 10 and 11, where these Cr and Mn depletions in the subsurface are visually more or less hindered by the presence of coarse Hf or Ta oxides.

To obtain some quantitative information concerning the zones modified chemically, a series of EDS spot analyses were performed in the outermost part of each alloy, just below the oxidation front. The obtained results led to the values of average and standard deviation for the weight contents (Table 2).

One can see that the Cr and Mn contents are significantly lowered, especially in the case of manganese (down to about 2 wt.%, against only down to 11.5 wt.% for chromium). This suggests that these contents, notably the Cr one (this is chromia, which is really protective against hot oxidation), can be considered as critical values. General oxidation of the whole alloys was probably imminent when the oxidation test was stopped.

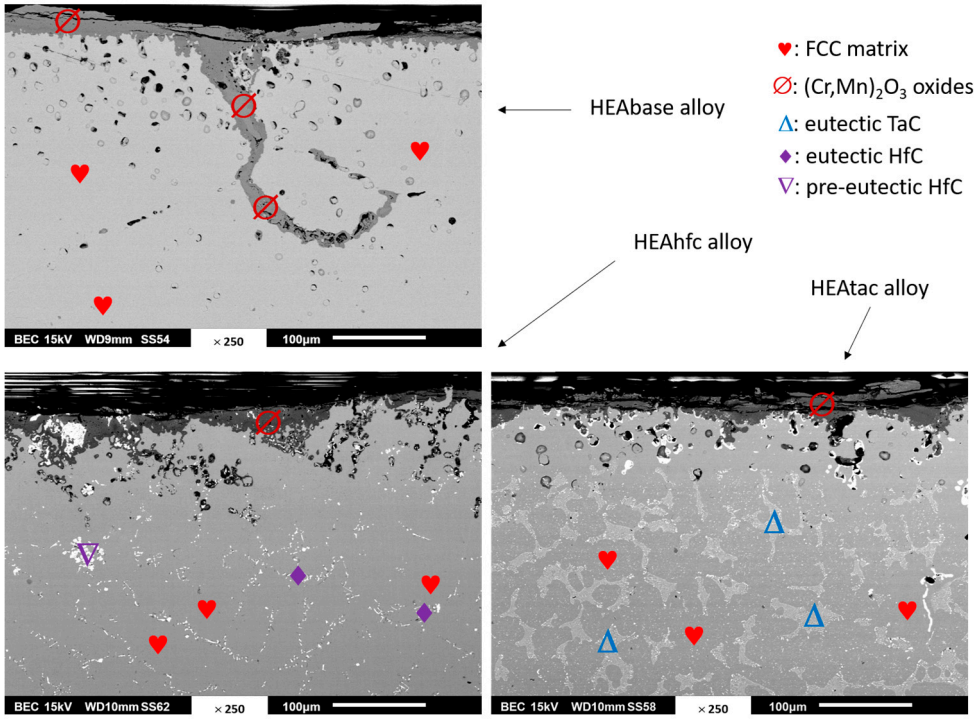

Figure 7. Low magnification SEM/BSE micrographs giving general views of the oxidized surfaces, subsurfaces and bulks.

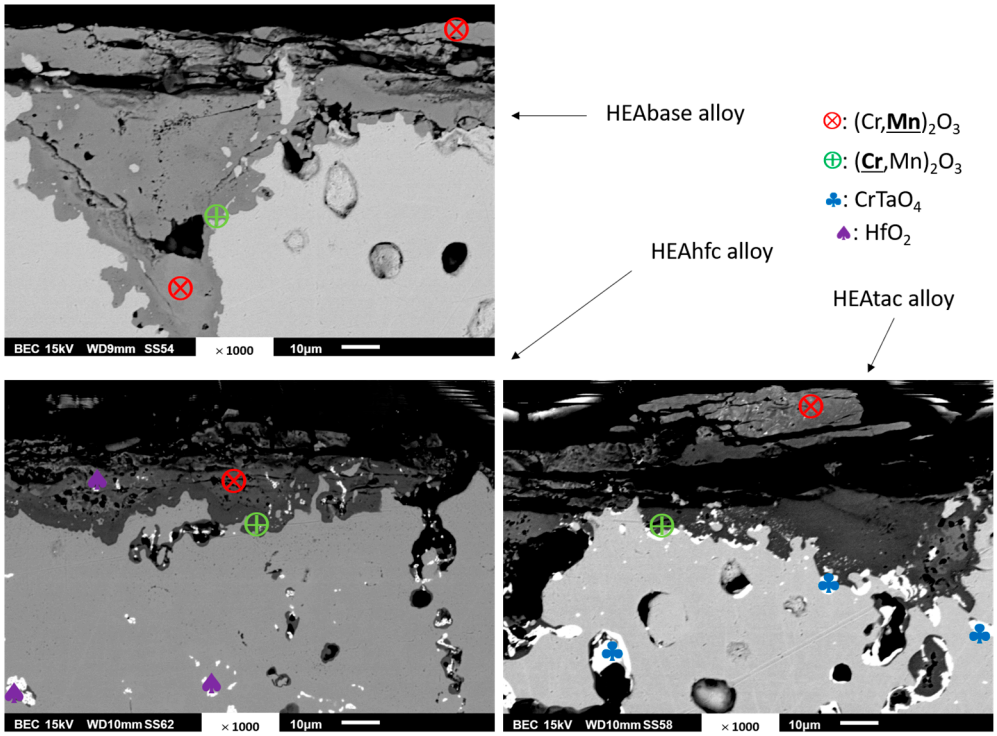

Figure 8. High-magnification SEM/BSE micrographs giving detailed views of the oxidized surfaces and subsurfaces, with the results of EDS spot analysis identification of the oxides.

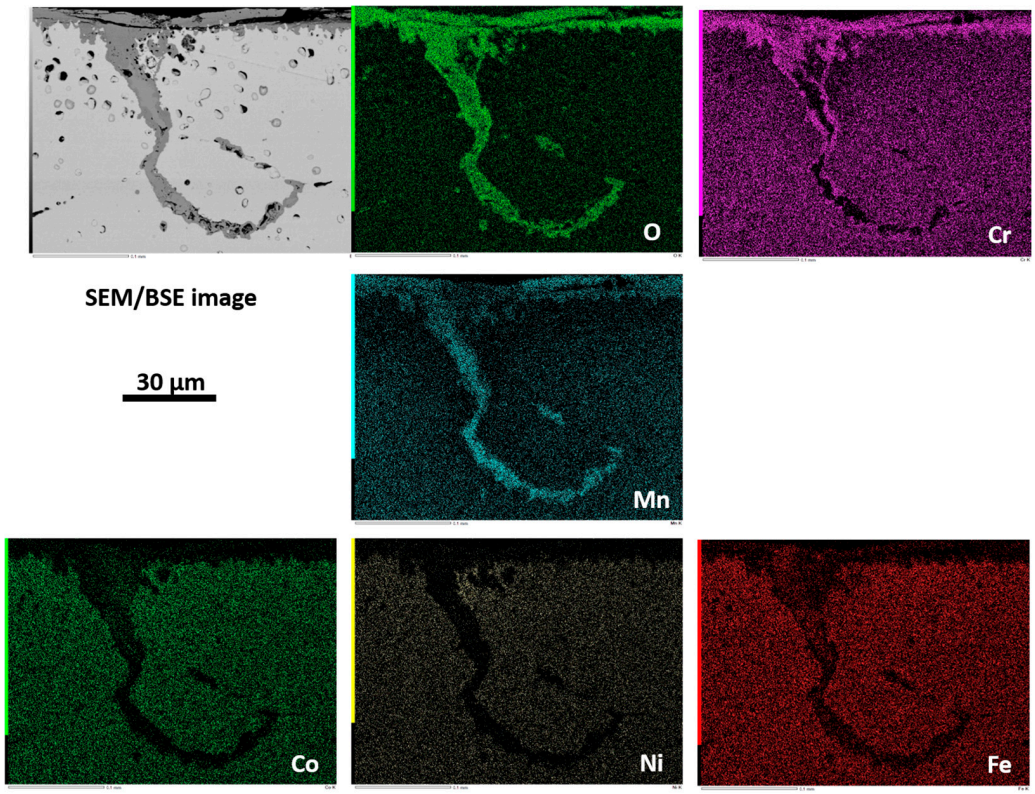

Figure 9. Elemental EDS cards of the oxidized surface and subsurface in the case of HEAbase.

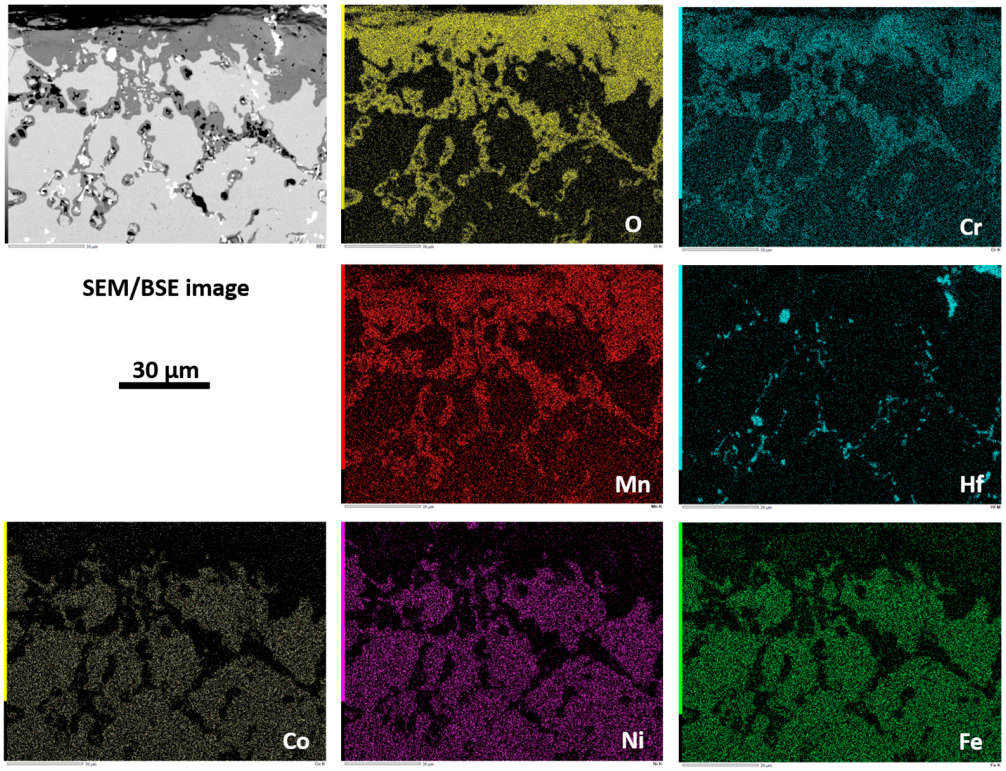

Figure 10. Elemental EDS cards of the oxidized surface and subsurface in the case of HEAhfc.

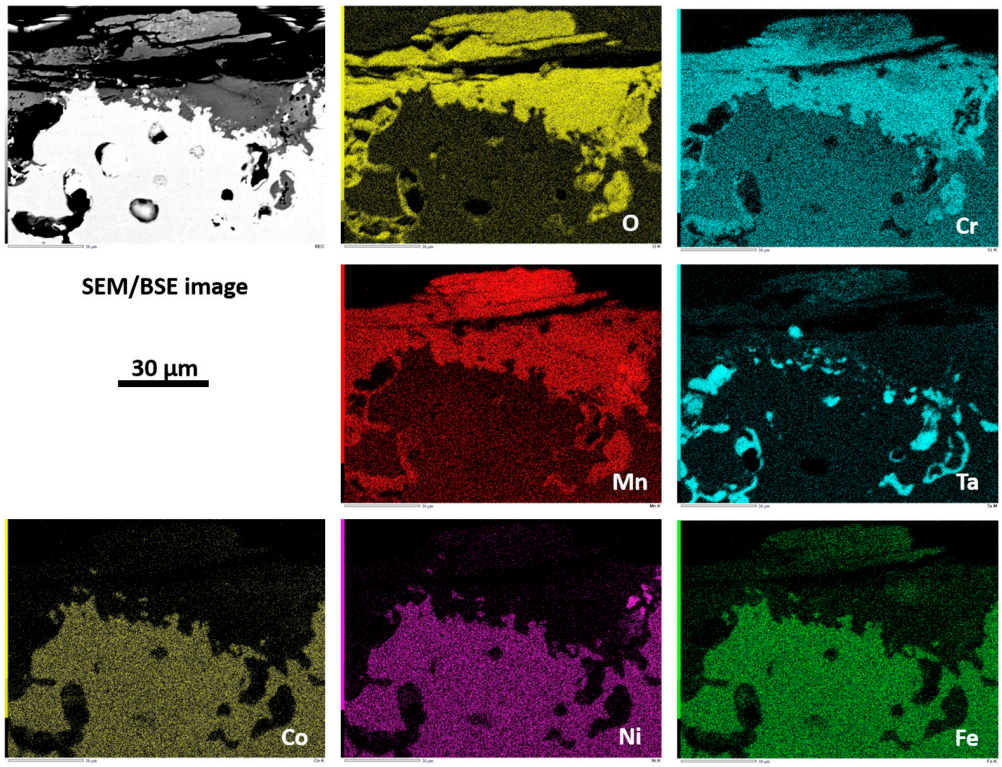

Figure 11. Elemental EDS cards of the oxidized surface and subsurface in the case of HEAtac.

Table 2. Chemical compositions in alloy very close to the interface with the external oxide scale (from five spot EDS analyses per alloy).

Extreme Surface (Contents in wt.%)		Cr	Mn	Fe	Co	Ni	Hf or Ta
HEAbase	Average	12.1	1.9	29.9	27.7	28.3	/
	Std dev.	0.5	0.1	0.3	0.3	0.3	/
HEAhfc	Average	11.0	2.5	27.8	28.9	29.9	0
	Std dev.	1.0	0.5	0.5	1.0	1.0	0
HEAtac	Average	11.7	1.6	29.4	27.0	30.0	0.3
	Std dev.	1.2	0.1	0.8	0.2	0.9	0.4

3.4. Three Points Bending Creep Tests

One (1100 °C, 10 MPa) creep test was carried out for each alloy. The obtained deformation curves (downward movement of the central point versus time) are presented in Figures 12–14 for the HEAbase alloy, the HEAhfc alloy and the HEAtac alloy, respectively. A common point between the three deformation curves is that the primary stage of creep was not finished when the temperature reached 1100 °C since, at this moment, the deformation rate was still decreasing. However, if the transition from the primary stage to the secondary stage was realized after less than 10 h (followed by a linear deformation) for the HEA alloy, the primary stage took more time for the two carbide-containing alloys; its duration was about 30 h for the HEAtac alloy, while it seems to be not yet finished after 150 h for the HEAhfc alloy.

To specify the deformation rate during the secondary creep stage, the derived values of central point displacement were calculated and plotted versus time in the same graphs. The deformation rates during the secondary stage are about 10 μm h^{-1} for the HEAbase alloy and about 2 μm h^{-1} for the HEAtac one. In the case of the HEAhfc alloy, the rate slightly decreases from 2 to less than 1 μm h^{-1} over about 150 h. This confirms that the secondary creep stage is, thus, not yet completed. With its rather fast deformation rate, the HEAbase sample came in contact with the apparatus base after almost 100 h (experiment was then stopped). The two alloys containing MC carbides are obviously much more creep-resistant, demonstrating the strengthening effect of the presence of the eutectic HfC and TaC carbides.

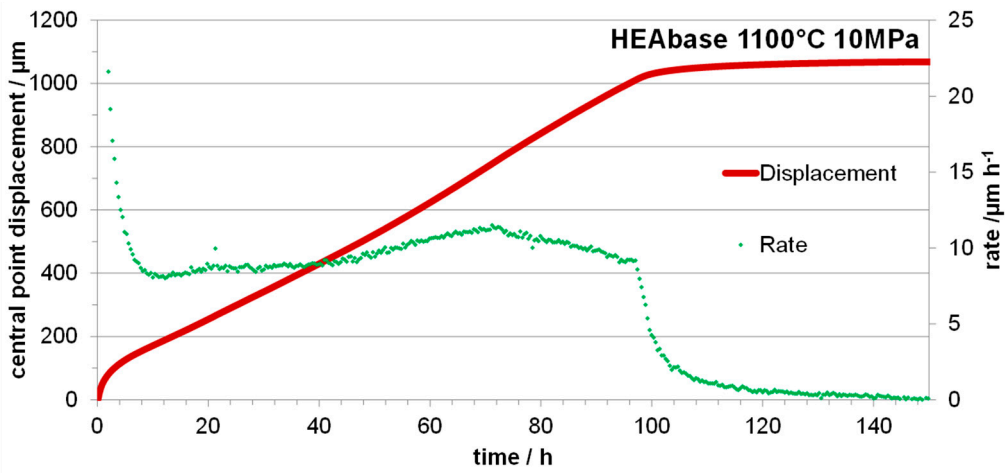

Figure 12. Deformation curve of the HEAbase alloy, superposed with the corresponding deformation rate evolution.

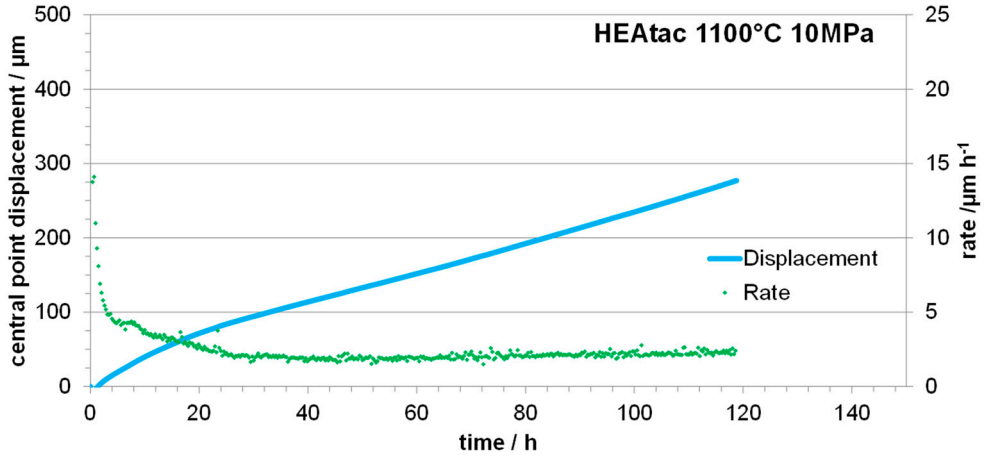

Figure 13. Deformation curve of the HEAhfc alloy, superposed with the corresponding deformation rate evolution.

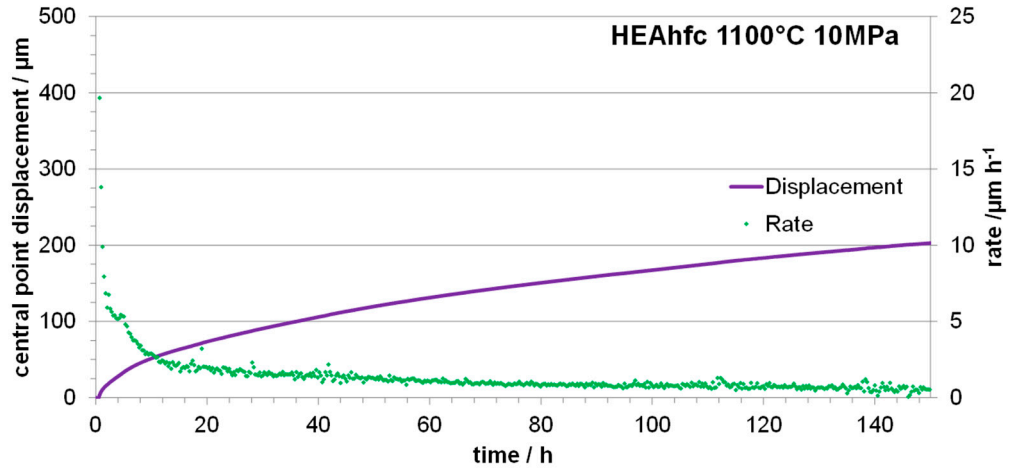

Figure 14. Deformation curve of the HEAtac alloy, superposed with the corresponding deformation rate evolution.

3.5. Comments on the Mechanisms of Oxidation and of Creep Deformation

The oxidation phenomena obviously involved principally chromium and manganese. This is evidenced first by the predominance of the oxides of Mn and Cr in the external and internal corrosion products. The impoverishment of the subsurface in these two elements and the low Cr and Mn contents in the outer part of alloy very close to the oxidation front (particularly Mn) are other consequences of the selective oxidation of both Mn and Cr. Cobalt, nickel and iron only played an anecdotal role in oxidation. Ni, Co and Fe were preserved from oxidation thanks to the more oxidable character of Cr and particularly of Mn. Indeed, at 1100 °C, the free enthalpies of formation of the corresponding oxides are ordered as follows (Ellingham's graph): Mn oxides < Cr oxides < Fe oxides < Co oxides < Ni oxides [29,30]. Some oxides involving Fe, Co or Ni were present only as traces. The other metals that were oxidized were hafnium and tantalum, known as easily oxidable elements.

Concerning the oxidation mechanisms, it appears obvious that a double diffusion acted for all alloys at 1100 °C in air. First, Cr and Mn diffused from the alloy to the oxidation front and formed the external scales. Second, oxygen diffused too, in the opposite direction, with the result being an inner oxide growth zone. This was particularly evidenced in some rare locations by grain boundary oxidation (deep oxide penetration in the HEAbase alloy) and by the in situ oxidation of hafnium (in HfO_2) or of tantalum (in Ta_2O_5 and $CrTaO_4$ after reaction with Cr_2O_3). This double simultaneous diffusion in two opposite directions led to an outward oxide thickening and an irregular inward oxidation progression. This second

growth mode (inward) allowed the formation of Mn and Cr oxides immersing some of the internal HfO_2 and $CrTaO_4$ oxides formed earlier. Except these formations of HfO_2 and $CrTaO_4$ followed by their inclusion in the Mn and Cr oxide growing inward, Hf and Ta did not detrimentally influence the global oxidation behavior of the alloys. The oxidation resistances of the HEAbase, HEAhfc and HEAtac alloys are poor and the degradation by oxidation can shorten life time significantly.

If this is chromium (or aluminum), which is usually selectively oxidized in superalloys in similar conditions of oxidation, here, external (and internal) selective oxidation also affects manganese. Furthermore, Mn is more involved in oxidation than Cr. The oxidation products are consequently complex and not homogeneous in compositions (oxides of both Mn and Cr in various proportions). Despite the continuous covering of the alloy by the external scale, because of the presence of multiple defects (heterogeneities and vacancies due to lack of stoichiometry), the protection brought by the external scale is much lower than in the case of the quasi-stoichiometric chromia. This is demonstrated first by significantly higher average thicknesses for the isothermal oxidation process (twice the chromia thickness usually observed for chromia-forming superalloys) and by the deterioration state of the external scale after post-isothermal cooling (obvious multiple shear ruptures and loss of oxide parts by spallation). In addition, the carbide-free HEA alloy is also affected by fast inward progress of internal oxidation initiated by the Mn enrichment of the grain boundaries (segregation at solidification), by the high reactivity of manganese with oxygen (very negative free enthalpy of the oxide formation) and by the easy oxygen diffusivity in Mn-rich oxides. Internal oxidation occurs too in the interdendritic spaces of the two carbide-containing alloys. But the tantalum oxides and hafnium oxides resulting from MC carbide oxidation act as barriers for oxygen diffusion, slowing down the progress of oxidation.

Due to their inaptitude to develop an external continuous oxide scale protective enough because of the seemingly unavoidable high presence of Mn in the scale, these alloys are, thus, not oxidation-resistant enough to achieve a long lifespan. When present, the TaC or HfC carbides also oxidize, internally, and this participates in the degradation of the alloys. But, on the other hand, they limit internal Mn oxidation. They have, thus, both a deleterious effect and a favorable effect. To close the comments about the hot oxidation behavior of these alloys, it is sure that the expected lifetime should be rather short (less than one hundred hours or only slightly more), an evident conclusion which can be verified later by longer exposures (if really useful). Therefore, in case of promising mechanical properties at high temperature, they need to be coated to protect them against hot oxidation.

Concerning the mechanical properties at high temperature, a significantly positive influence of the MC carbides on the creep resistance was evidenced here by the comparison with the carbide-free HEA. HfC and TaC carbides are very hard particles and very resistant mechanically at high temperatures. Further, their particular morphology (Chinese script) produces a strong blocking effect between neighbor dendrites and between neighbor grains. This effect persists a long time at high temperature because of the great resistance of these MC carbides against fragmentation and the resulting loss of carbide continuity. The superiority of the HfC- or TaC-strengthened versions of the CoNiFeMnCr HEA base alloy was assumed, and it is now verified. In the HEAbase alloy, dislocations freely moved and continuously produced many sliding steps, which added up to each other, this resulting in grain-to-grain sliding and then in the macroscopic viscous-plastic deformation of the alloy. With the interdendrite and intergrain lockdown due to the HfC or TaC carbides imbricated with matrix, the deformation is much slower. These carbides bring important resistance against mechanical failure. Unfortunately, the present creep results of the HEAtac and HEAfhc alloys cannot be compared to published results obtained for commercial superalloys. Indeed, such comparison requires that the commercial alloys be tested at 1100°C and 10 MPa in the same conditions as here, i.e., centered three-point flexural solicitation mode, same space between the two bottom supports (12 mm), similar sample thickness, etc. To our knowledge, no results respecting these conditions are available in

the literature. Comparisons with commercial alloys would be easier to conduct between traction creep results but this is not possible for the moment because of a lack of the adequate testing machine.

4. Conclusions

Inspired by recent good results obtained with polycrystalline MC-strengthened cobalt-based or nickel-based alloys and superalloys, this work was undertaken to explore the potential properties at 1100 °C of new alloys similarly designed. These ones associate an equimolar CoNiFeMnCr matrix (known for its high intrinsic strength at various temperatures) and interdendritic heat-resistant script-like eutectic MC carbides (efficient strengthening particles at high temperature). The obtained results are contrasted since major improvement of creep resistance was achieved thanks to TaC and HfC by comparison with the carbide-free reference alloy. These promising creep results will be enriched by uniaxial tensile creep tests as soon as an adequate creep machine is installed in the laboratory. In contrast, the hot oxidation resistances of the three alloys are low. The principal responsible element is neither Ta nor Hf but Mn. It was effectively observed that manganese took a major part of the oxide formation—externally and internally—and obstructed the chromia-forming role of Cr. Due to the rather high level of Mn content in the Cantor's alloy and its derivatives, chromia failed to form and a not so protective external scale developed instead. Improving considerably the oxidation resistance is the key to benefiting from the (by MC) reinforcement of these alloys. Applying a protective coating to these alloys can be a solution.

Author Contributions: Conceptualization, P.B.; methodology, P.B.; software, L.A.; validation, P.B. and L.A.; formal analysis, P.B.; investigation, P.B.; resources, L.A.; data curation, P.B. and L.A.; writing—original draft preparation, P.B.; writing—review and editing, P.B.; visualization, P.B.; supervision, P.B.; project administration, P.B.; funding acquisition, not applicable. All authors have read and agreed to the published version of the manuscript.

Funding: This research received no external funding.

Institutional Review Board Statement: Not applicable.

Informed Consent Statement: Not applicable.

Data Availability Statement: Data are contained within the article.

Acknowledgments: The authors wish to thank their colleagues for their technical help: Pierre-Jean Panteix (for the exposures of samples in furnace) and Ghouti Medjahdi (who launched the XRD runs).

Conflicts of Interest: The authors declare no conflicts of interest.

References

1. Wilson, P.; Field, R.; Kaufman, M. The use of diffusion multiples to examine the compositional dependence of phase stability and hardness of the Co-Cr-Fe-Mn-Ni high entropy alloy system. *Intermetallics* **2016**, *75*, 15–24. [CrossRef]
2. Dąbrowa, J.; Kucza, W.; Cieślak, G.; Kulik, T.; Danielewski, M.; Yeh, J.-W. Interdiffusion in the FCC-structured Al-Co-Cr-Fe-Ni high entropy alloys: Experimental studies and numerical simulations. *J. Alloys Compd.* **2016**, *674*, 455–462. [CrossRef]
3. Shafiei, A. Design of eutectic high entropy alloys in Al-Co-Cr-Fe-Ni system. *Met. Mater. Int.* **2021**, *27*, 127–138. [CrossRef]
4. Stepanov, N.; Shaysultanov, D.; Tikhonovsky, M.; Zherebtsov, S.-V. Structure and high temperature mechanical properties of novel non-equiatomic Fe-(Co, Mn)-Cr-Ni-Al-(Ti) high entropy alloys. *Intermetallics* **2018**, *102*, 140–151. [CrossRef]
5. Zhao, Y.; Yang, T.; Zhu, J.; Chen, D.; Yang, Y.; Hu, A.; Liu, C.-T.; Kai, J.-J. Development of high-strength Co-free high-entropy alloys hardened by nanosized precipitates. *Scr. Mater.* **2018**, *148*, 51–55. [CrossRef]
6. Nagase, T.; Todai, M.; Nakano, T. Liquid Phase Separation in Ag-Co-Cr-Fe-Mn-Ni, Co Cr-Cu-Fe-Mn-Ni and Co-Cr-Cu-Fe-Mn-Ni-B High Entropy Alloys for Biomedical Application. *Crystals* **2020**, *10*, 527. [CrossRef]
7. Bracq, G.; Laurent-Brocq, M.; Perrière, L.; Pirès, R.; Joubert, J.-M.; Guillot, I. The fcc solid solution stability in the Co-Cr-Fe-Mn-Ni multi-component system. *Acta Mater.* **2017**, *128*, 327–336. [CrossRef]
8. Liu, S.F.; Wu, Y.; Wang, H.T.; He, J.Y.; Liu, J.B.; Chen, C.X.; Wang, H.; Liu, X.J.; Lu, Z.P. Stacking fault energy of face-centered-cubic high entropy alloys. *Intermetallics* **2018**, *93*, 269–273. [CrossRef]

9. Wei, D.; Li, X.; Jiang, J.; Heng, W.; Koizumi, Y.; Choi, W.-M.; Lee, B.-J.; Kim, H.S.; Kato, H.; Chiba, A. Novel Co-rich high performance twinning-induced plasticity (TWIP) and transformation-induced plas-ticity (TRIP) high-entropy alloys. *Scr. Mater.* **2019**, *165*, 39–43. [CrossRef]
10. Dąbrowa, J.; Stygar, M.; Mikuła, A.; Knapik, A.; Mroczka, K.; Tejchman, W.; Danielewski, M.; Martin, M. Synthesis and microstructure of the $(Co,Cr,Fe,Mn,Ni)_3O_4$ high entropy oxide characterized by spinel structure. *Mater. Lett.* **2018**, *216*, 32–36. [CrossRef]
11. Teramoto, T.; Yamada, K.; Ito, R.; Tanaka, K. Monocrystalline elastic constants and their temperature dependences for equi-atomic Cr-Mn-Fe-Co-Ni high-entropy alloy with the face-centered cubic structure. *J. Alloys Compd.* **2018**, *777*, 1313–1318. [CrossRef]
12. Kauffmann, A.; Stüber, M.; Leiste, H.; Ulrich, S.; Schlabach, S.; Szabó, D.V.; Seils, S.; Gorr, B.; Chen, H.; Seifert, H.-J.; et al. Combinatorial exploration of the high entropy alloy system Co-Cr-Fe-Mn-Ni. *Surf. Coat. Technol.* **2017**, *325*, 174–180. [CrossRef]
13. Choi, W.-M.; Jung, S.; Jo, Y.H.; Lee, S.; Lee, B.-J. Design of new face-centered cubic high entropy alloys by thermodynamic calculation. *Met. Mater. Int.* **2017**, *23*, 839–847. [CrossRef]
14. Kawamura, M.; Asakura, M.; Okamoto, N.L.; Kishida, K.; Inui, H.; George, E.P. Plastic deformation of single crystals of the equiatomic Cr-Mn-Fe-Co-Ni high-entropy alloy in tension and compression from 10 K to 1273 K. *Acta Mater.* **2021**, *203*, 116454. [CrossRef]
15. Haase, C.; Tang, F.; Wilms, M.B.; Weisheit, A.; Hallstedt, B. Combining thermodynamic modeling and 3D printing of elemental powder blends for high-throughput investigation of high-entropy alloys—Towards rapid alloy screening and design. *Mater. Sci. Eng. A* **2017**, *688*, 180–189. [CrossRef]
16. Ye, Q.; Feng, K.; Li, Z.; Lu, F.; Li, R.; Huang, J.; Wu, Y. Microstructure and corrosion properties of CrMnFeCoNi high entropy alloy coating. *Appl. Surf. Sci.* **2017**, *396*, 1420–1426. [CrossRef]
17. Song, H.; Ma, Q.; Zhang, W.; Tian, F. Effects of vacancy on the thermodynamic properties of Co-Cr-Fe-Mn-Ni high-entropy alloys. *J. Alloys Compd.* **2021**, *885*, 160944. [CrossRef]
18. Varvenne, C.; Luque, A.; Curtin, W.A. Theory of strengthening in fcc high entropy alloys. *Acta Mater.* **2016**, *118*, 164–176. [CrossRef]
19. Shafiei, A. Simple Approach to Model the Strength of Solid-Solution High Entropy Alloys in Co-Cr-Fe-Mn-Ni System. *Strength Mater.* **2022**, *54*, 705–716. [CrossRef]
20. Kucza, W.; Dąbrowa, J.; Cieślak, G.; Berent, K.; Kulik, T.; Danielewski, M. Studies of "sluggish diffusion" effect in Co-Cr-Fe-Mn-Ni, Co-Cr-Fe-Ni and Co-Fe-Mn-Ni high entropy alloys; determination of tracer diffusivities by combinatorial approach. *J. Alloys Compd.* **2017**, *731*, 920–928. [CrossRef]
21. Chen, W.; Zhang, L. High-Throughput Determination of Interdiffusion Coefficients for Co-Cr-Fe-Mn-Ni High-Entropy Alloys. *J. Phase Equilibria Diffus.* **2017**, *38*, 457–465. [CrossRef]
22. Berthod, P.; Conrath, E. Mechanical and chemical properties at high temperature of {M-25Cr}-based alloys containing hafnium carbides (M=Co, Ni or Fe): Creep behavior and oxidation at 1200 °C. *J. Mater. Sci. Technol. Res.* **2014**, *1*, 7–14. [CrossRef]
23. Michon, S.; Aranda, L.; Berthod, P.; Steinmetz, P. High temperature evolution of the microstructure of a cast cobalt base superalloy. Consequences on its thermomechanical properties. *La Rev. De Métallurgie-CIT/Sci. Et Génie Des Matériaux* **2004**, *101*, 651–662. [CrossRef]
24. Stepanov, N.D.; Yurchenko, N.Y.; Tikhonovsky, M.A.; Salishchev, G.A. Effect of carbon content and annealing on structure and hardness of the CoCrFeNiMn-based high entropy alloys. *J. Alloys Compd.* **2016**, *687*, 59–71. [CrossRef]
25. Berthod, P. As-Cast microstructures of high entropy alloys designed to be TaC-strengthened. *J. Met. Mater. Res.* **2022**, *5*, 1–10. [CrossRef]
26. Ferrari, A.; Koermann, F. Surface segregation in Cr-Mn-Fe-Co-Ni high entropy alloys. *Appl. Surf. Sci.* **2020**, *533*, 147471. [CrossRef]
27. Berthod, P. Influence of chromium carbides on the high temperature oxidation behavior and on chromium diffusion in nickel-base alloys. *Oxid. Met.* **2007**, *68*, 77–96. [CrossRef]
28. Kim, Y.-K.; Joo, Y.-A.; Kim, H.S.; Lee, K.-A. High temperature oxidation behavior of Cr-Mn-Fe-Co-Ni high entropy alloy. *Intermetallics* **2018**, *98*, 45–53. [CrossRef]
29. Sabat, K.C.; Rajput, P.; Paramguru, R.K.; Bhoi, B.; Mishra, B.K. Reduction of Oxide Minerals by Hydrogen Plasma: An Overview. *Plasma Chem Plasma Process* **2014**, *34*, 1–23. [CrossRef]
30. Available online: https://commons.wikimedia.org/wiki/File:Ellingham_Richardson-diagram_english.svg (accessed on 30 December 2023).